JGR Space Physics

RESEARCH ARTICLE
10.1029/2025JA033818

Mesoscale Ionospheric Structures and Very Large Geomagnetic Disturbances at High Latitudes

Mark J. Engebretson[1], James M. Weygand[2], Yukitoshi Nishimura[3], Mark B. Moldwin[4], Erik S. Steinmetz[1], Jesus A. Ochoa[1], Vyacheslav A. Pilipenko[5], and Jesper Gjerloev[6]

[1]Department of Physics, Augsburg University, Minneapolis, MN, USA, [2]UCLA Department of Earth Planetary and Space Sciences, Los Angeles, CA, USA, [3]Department of Electrical and Computer Engineering and Center for Space Physics, Boston University, Boston, MA, USA, [4]Department of Climate and Space Sciences and Engineering, University of Michigan, Ann Arbor, MI, USA, [5]Space Research Institute, Moscow, Russian Federation, [6]Johns Hopkins University Applied Physics Laboratory, Laurel, MD, USA

Abstract Auroral substorms that move from auroral (<70°) to polar (>70°) magnetic latitudes (MLAT) are known to occur preferentially when a high-speed solar wind stream passes by Earth. We report here on observations that occurred during a ~75-min interval with high-speed solar wind on 28 November 2022 during which auroral arcs and very large geomagnetic disturbances (GMDs), also known as magnetic perturbation events (MPEs), with amplitude >9 nT/s = 540 nT/min moved progressively poleward at eight stations spanning a large region near and north of Hudson Bay, Canada shortly before midnight local time. Sustained GMD activity with amplitudes >3 nT/s appeared at each station for durations from 13 to 25 min. Spherical Elementary Currents Systems maps showed the poleward movement of a large-scale westward electrojet as well as mesoscale electrojet structures and highly localized up/down pairs of vertical currents near these stations when the largest GMDs were observed. This study is consistent with other recent studies showing that very large poleward-progressing GMDs can occur under high Vsw conditions, but is the first to document the sustained occurrence of large GMDs over such a wide high-latitude region.

Key Points:

- >9 nT/s geomagnetic disturbances (GMDs) were observed at eight high latitude sites in Arctic Canada during a high-speed solar wind stream
- Sustained >3 nT/s GMD activity appeared at each station with durations from 13 to 25 min during the expansion phase of a substorm
- Highly localized, transient, and intense up/down current pairs produced these GMDs and associated localized electrojets

Supporting Information:

Supporting Information may be found in the online version of this article.

Correspondence to:

M. J. Engebretson,
engebret@augsburg.edu

Citation:

Engebretson, M. J., Weygand, J. M., Nishimura, Y., Moldwin, M. B., Steinmetz, E. S., Ochoa, J. A., et al. (2025). Mesoscale ionospheric structures and very large geomagnetic disturbances at high latitudes. *Journal of Geophysical Research: Space Physics*, *130*, e2025JA033818. https://doi.org/10.1029/2025JA033818

Received 4 FEB 2025
Accepted 28 JUL 2025

Author Contributions:

Conceptualization: Mark J. Engebretson, James M. Weygand, Yukitoshi Nishimura
Data curation: Erik S. Steinmetz, Jesper Gjerloev
Formal analysis: Mark J. Engebretson, James M. Weygand, Yukitoshi Nishimura
Funding acquisition: Mark J. Engebretson, James M. Weygand, Yukitoshi Nishimura, Mark B. Moldwin
Investigation: Mark J. Engebretson, James M. Weygand, Yukitoshi Nishimura, Mark B. Moldwin, Jesus A. Ochoa, Vyacheslav A. Pilipenko, Jesper Gjerloev
Methodology: Mark J. Engebretson, James M. Weygand, Yukitoshi Nishimura

1. Introduction

The latitudinal range of Earth's auroras and the most prominent of their variations, the auroral substorm, have been a subject of study for decades, beginning with the pioneering efforts of, for example, Akasofu (1964). Correlations between the onset and intensity of auroral and geomagnetic activity and features of the interplanetary magnetic field (IMF) and solar wind were also discovered early in the space age, for example, beginning with the discovery by Fairfield and Cahill (1966) that a southward IMF impinging on Earth's magnetosphere could spark sudden increases in activity. The latitudinal range within which the auroral oval occurs has been found to vary significantly, contracting toward the polar cap during conditions of low geomagnetic activity and expanding equatorward during intervals of high activity. During the substorm expansion phase, auroras and a westward electrojet move poleward (Kisabeth and Rostoker, 1974; Troshichev et al., 1974). A particular class of substorms, high-latitude substorms, begin in the auroral zone and then propagate to high latitudes (Akasofu, 2004; Despirak et al., 2014; Doolittle et al., 1998; Gussenhoven, 1982). A characteristic of the driving of the high-latitude substorms studied in the latter three papers that distinguishes them from the majority of substorms is that they occurred during high speed solar wind streams.

The impact of externally triggered extreme geomagnetic activity on technological infrastructure, large currents induced in long-distance telegraph lines, was first noted in association with the "Carrington event" (Carrington, 1859), when intense low-latitude auroras appeared shortly after an unusually strong solar flare. Similar large, rapid perturbations in magnetic fields, known as geomagnetic disturbances (GMDs), that often occur during such periods of extreme geomagnetic activity (Boteler, 2019; Hapgood, 2019; Love et al., 2019) are now understood to produce damaging geomagnetically induced currents (GICs) that can couple to long-distance electrical power lines, pipelines, and even undersea cables (Ngwira & Pulkkinen, 2019).

Recent statistical studies of GMDs by Milan et al. (2023) and Engebretson, Yang, et al. (2024) reported a strong association between large GMDs and high solar wind velocity (Vsw) values. Milan et al. (2023) used 1-min cadence observations from all ground-based magnetometers in the SuperMAG (Gjerloev, 2012) database from 1995 through 2020. As a proxy for large dB/dt values in each component, they identified minute-to-minute

changes in any magnetic field component that exceeded 300 nT. They found that most such events occurred predominantly at >50° MLAT, and that pre-midnight GMDs occurred at all phases of the solar cycle but maximized in the declining phase. Figure 3 of Milan et al. (2023) showed that the occurrence rate of these events in three different local time sectors peaked during the years when Vsw distributions were the highest.

Engebretson, Yang, et al. (2024) used 0.5-s cadence observations from five stations in the MACCS and AUTUMNX arrays from 65° to 75° MLAT from 2011 through 2022 to identify all large and extreme GMDs with greater than 6 nT/s and 20 nT/s (360 nT/min and 1200 nT/min, respectively). This study found that both GMD populations maximized during the declining phase of the solar cycle, and that in particular the occurrence of >20 nT/s GMD was strongly associated with high Vsw values (their Figure 4). Engebretson, Yang, et al. (2024) also showed that GMD occurrences in two earlier long-term studies peaked during the declining phase: Kellinsalmi et al. (2022) compiled the distribution of >1 nT/s GMDs observed at Sodankylä, Finland from 1996 through 2018, and Marshall et al. (2011) presented GMD activity index data from 1985 through 2009 from several sites across Australia.

It is important to note that sparsely populated eastern Arctic Canada is not particularly vulnerable to damage from GICs. No long-distance conductors are present; instead, each of its towns has its own electrical power utility. However, the two-dimensional magnetometer coverage in eastern Arctic Canada has been useful for what was labeled "discovery research" in the 2024 Solar and Space Physics Decadal Survey (National Academies of Sciences, Engineering, and Medicine, 2024) in many studies of high latitude phenomena, including several recent studies of GMDs, especially with regard to their mesoscale features and physical causes.

This study provides an additional example of the close associations between large isolated GMDs and mesoscale ionospheric features that have been reported in recent studies by Weygand et al. (2021, 2022), McCuen et al. (2023), Engebretson, Gaffaney, et al. (2024), and Shi et al. (2025).

Weygand et al. (2021) used Spherical Elementary Current Systems (SECS) maps to characterize the locations of 279 GMD events with amplitude >6 nT/s observed at two stations in Arctic Canada during 2015 and 2017 relative to eastward or westward electrojets and downward or upward region 1 and region 2 field-aligned currents. They examined four events in detail, with varying contexts of storm and substorm conditions. In each case, the horizontal ionospheric currents intensified and highly localized and transient vertical currents appeared over the observing station, and in both the events for which auroral images were available, brightening overhead arcs were observed.

Weygand et al. (2022) examined two north-south auroral streamer events and simultaneous fast earthward flows in the near magnetotail observed by the THEMIS spacecraft. In both cases SECS analyses revealed a localized up/down current pair beneath the streamer, a localized horizontal current between them, and a surrounding current vortex.

McCuen et al. (2023) and Engebretson, Gaffaney, et al. (2024) reported similarly localized ionospheric currents and aurorae in association with large GMDs, but also presented evidence that they were closely associated with dipolarization fronts observed at synchronous orbit (McCuen et al., 2023) or dipolarizing flux bundles observed by THEMIS in the near magnetotail (Engebretson, Gaffaney, et al., 2024).

More recently, Shi et al. (2025) presented a detailed examination of a GMD event that occurred in a region in the upper Midwest United States during a 3-week interval in 2011 when both geomagnetic and geoelectric fields were recorded at a 1-s cadence at 8 stations in a dense array as part of the EarthScope project. This data set provided unprecedented spatial details of both the magnetic perturbations and the geoelectric fields, and the inferred ionospheric currents were consistent with ionospheric equivalent and vertical currents derived from SECS analysis of other magnetometers in the region, but excluding these 8 stations.

In this study, we use magnetometer data from a two-dimensional array of magnetometers in eastern Arctic Canada to show the widespread occurrence of >9 nT/s GMDs and sustained tens of minute intervals of >3 nT/s GMDs at very high latitudes, and augment it with all-sky imager data and Spherical Elementary Current Systems (SECS) maps in order to provide physical insight into the mesoscale features associated with them. Section 2 introduces the ground magnetometers and all-sky imagers used in this study. Section 3.1 presents the large-scale solar wind and magnetospheric context of this event, Section 3.2 presents the magnetic field data, and Section 3.3 presents auroral imager data and SECS maps to show the smaller scale context and features of these events. Section 4

Table 1
Locations of the Magnetometer Stations Used in This Study

Array	Station	Code	Geog. Lat.	Geog. Lon.	CGM Lat.	CGM Lon.	UT of Mag Midnight
MACCS	Gjoa Haven	GJO	68.6°	264.2°	76.3°	−29.3°	06:25
	Igloolik	IGL	69.3°	278.2°	77.1°	−5.2°	04.55
	Repulse Bay	RBY	66.5°	273.8°	74.6°	−12.6°	05:23
	Coral Harbor	CHB	64.2°	276.7°	72.4°	−7.8°	05:05
	Cape Dorset	CDR	64.2°	283.4°	72.1°	2.6°	04:25
CARISMA	Taloyoak	TAL	69.5°	266.5°	77.2°	−25.7°	06:11
	Rankin Inlet	RAN	62.8°	267.9°	71.2°	−21.8°	05:57
CANMOS	Baker Lake	BLC	64.3°	264.0°	72.4°	−28.2°	06:21
BGS	Resolute Bay	RES	74.9°	265.1°	82.0°	−31.6°	06:33
Interstation Distances:		GJO-TAL		136 km			
		RAN-CDR		786 km			

Note. Geographic and corrected geomagnetic (CGM) latitude and longitude are shown, as well as the universal time (UT) of local magnetic midnight. Distances between two selected pairs of stations are also presented. CGM coordinates were calculated for epoch 20221128 at 100 km altitude, using http://sdnet.thayer.dartmouth.edu/aacgm/aacgm_calc.php#AACGM.

discusses the connections of this event to earlier studies, and Section 5 summarizes our findings and their implications.

2. Instrumentation

Vector magnetometer data used in this study were recorded at nine high magnetic latitude stations in the MACCS (Engebretson et al., 1995), CARISMA (Mann et al., 2008), and CANMOS (Nikitina et al., 2016) arrays and at the British Geological Survey Resolute Bay site in eastern Arctic Canada with corrected geomagnetic latitude (CGM Lat) from 71.2° to 82.0° and magnetic longitude between −32° and +3°, as detailed in Table 1 and Figure 1. MACCS data were sampled at a 2 Hz cadence; CARISMA, CANMOS, and RES data were sampled at a 1 Hz cadence. Derivatives were calculated using the Lagrangian 3-point derivative approximation for digitally sampled data, $dB/dt[i] = (B[i+1] - B[i-1])/2\Delta t$, which provides timing at the center time $t[i]$ for both sampling rates. All magnetometer data are presented in local magnetic coordinates with sensor axes oriented as follows: X: magnetic north, Y: magnetic east, and Z: vertically down. This study also makes use of all-sky white-light images produced by the THEMIS imagers located at Rankin Inlet and Taloyoak (Donovan et al., 2006; Mende et al., 2008).

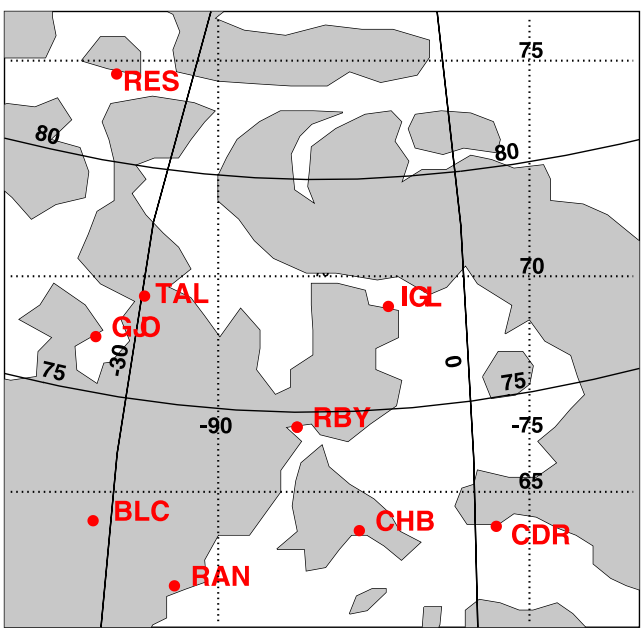

Figure 1. Map of ground magnetometer stations used in this study. Dotted lines show geographic latitude and longitude, and solid lines show corrected geomagnetic latitude and longitude. A portion of Hudson Bay is visible at the southern edge of the map.

3. Observations

3.1. Background Conditions

The context of this event is shown in Figure 2, a composite of OMNI IMF and solar wind data time shifted to the nose of the bow shock, the SMU and SML auroral activity indices (SuperMAG versions of the AU and AL indices), and the SYM/H index, from 04:30 to 06:00 UT on this day. Panel a shows that the IMF Bx component was negative near −7 nT from 05:14 UT to beyond 06:00 UT, the By component was strongly positive (~5–~8 nT) from 04:40 to beyond 06:00 UT, and the Bz component was <−5 nT from 04:30 to 05:13 UT and positive near +5 nT from 05:15 to ~05:45 UT. The OMNI solar wind velocity (Vsw), number density (Nsw) and dynamic pressure (Psw) are shown

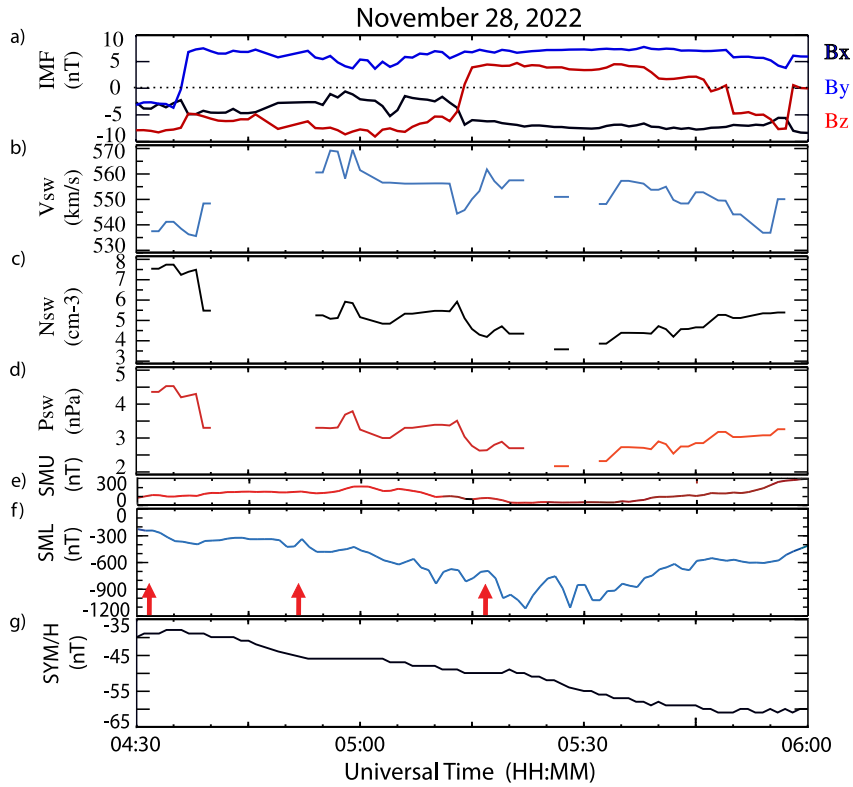

Figure 2. Time-shifted interplanetary magnetic field (panel a), solar wind velocity, density, and dynamic pressure (panels b–d) each from the OMNI database, and the SMU, SML, and SYM/H magnetic activity indices (panels e–g) from 04:30 to 06:00 UT 28 November 2022. The onset times of the three substorms identified in the SuperMAG Newell & Gjoerloev list are indicated by red arrows at the bottom of panel (f).

only intermittently; they indicate after 05:00 UT an elevated Vsw (~550 km/s), Nsw between ~4 and 6 cm^{-3}, and Psw between ~2 and 4 nPa.

THEMIS/Artemis-1, located upstream of Earth at 05:30 UT at $X = 32.4\ R_E$, $Y = 47.5\ R_E$, and $Z = -15.8\ R_E$ in GSM coordinates, observed similar variations in each IMF component at 05:08 UT, approximately 5 min before they occurred in the time-shifted OMNI data and consistent with the ~4 min time shift from the THEMIS/Artemis-1 location to the nose of the bow shock (not shown). Vsw dropped gradually from 540 km/s at 5:15 UT to 520 km/s at 06:00 UT, values slightly lower than OMNI values of ~560 and ~550 km/s, respectively.

The SMU index (panel e of Figure 2), an indicator of eastward electrojet activity, showed modest changes approximately opposite in sign to the IMF Bz component. The SML index (panel f) showed a slowly increasing level of westward electrojet activity from 04:30 to 05:30 UT with a minimum value near −1100 nT, after which the activity diminished more rapidly. Three rapid but short-lived drops in SML coincided approximately with the times of three substorm onsets identified using the Newell and Gjerloev (2011) criteria and included on the set of substorm onset lists presented on the SuperMAG web site (https://supermag.jhuapl.edu/substorms/), indicated by the red arrows, with drops of −100, −150, and −300 nT, respectively. The SYM/H index (panel g) fell slowly to a minimum value of −61 nT at 05:50 UT, after which time it gradually increased to −32 nT at 12:00 UT (not shown).

3.2. Ground-Based Magnetometer Observations

Figure 3 shows three components of the magnetic field observed at four representative stations: two of the highest latitude stations (GJO and TAL) and two of the lowest latitude stations (RAN and CDR) from 04:30 to 06:00 UT on this day. Also included in the bottom panels at each station are superposed color-coded plots of the time

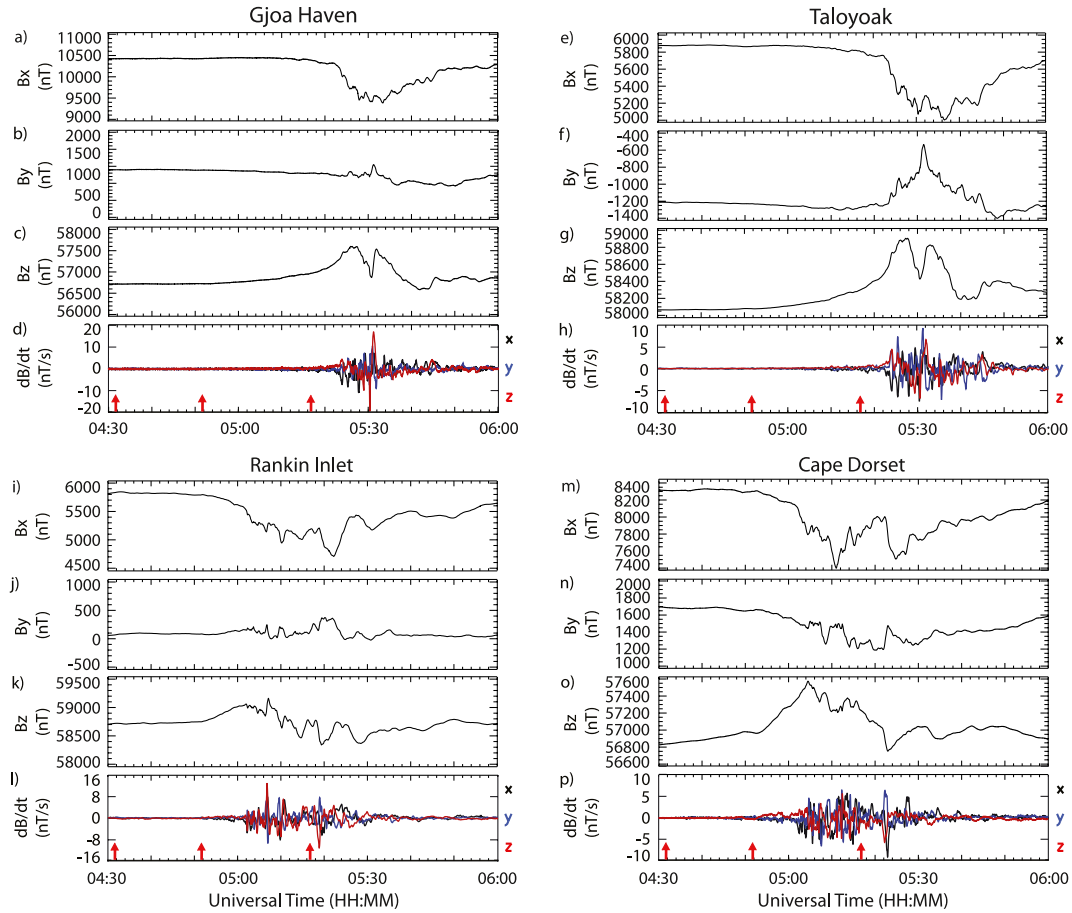

Figure 3. Magnetic field data and their derivatives in local geomagnetic coordinates at Gjoa Haven (panels a–d), Taloyoak (panels e–h), Rankin Inlet (panels i–l), and Cape Dorset (panels m–p), respectively, from 04:30 to 06:00 UT 28 November 2022. The onset times of the three substorms identified in the SuperMAG Newell & Gjoerloev list are indicated by red arrows in the bottom of panels (d, h, l, and p).

derivatives of each component, and the times of the three substorm onsets shown in Figure 2. Similar magnetic field plots for the other stations are included in the Supporting Information S1.

From 04:00 (not shown) to 04:50 UT, the magnetic field was roughly constant at all nine stations in the region bordering Hudson Bay and poleward of it, as shown in Figure 1. Near 04:52 UT, a 700–1100 nT negative bay began at the four lowest latitude stations (between 71.2° and 72.4°). A negative bay began at RBY (74.6°) 10 min later, near 05:00 UT, and at the four higher latitude stations (between 76.3° and 82.0°) 900–1250 nT negative bays began only near 05:10 UT. The times of the minima of the negative bays ranged from 05:10 to 05:22 UT for the five southernmost stations and from 05:28 to 05:40 UT for the four higher latitude stations.

Only slow variations in each component occurred from 05:10 to 05:22 UT at GJO and TAL, located 136 km apart (panels a–c and e–g), and derivatives in all three components were below 1 nT/s (panels d and h). The simultaneous onset of a significant drop (negative bay) in Bx at 05:22 UT can be seen in panels a and e, and nearly simultaneous Bx variations, but with smaller amplitude at TAL, were evident until 05:34 UT. The Bx component at GJO began a recovery toward earlier levels at 05:34 UT, while the recovery at TAL began slightly later, near 05:37 UT. Variations in the By component between 05:24 and 05:34 UT were also nearly simultaneous and roughly 2 times larger at TAL, but similar variations in the Bz component were ~50% larger at GJO. Derivative amplitudes in all three components at both stations increased rapidly at 05:23 UT (panels d and h), peaked at times corresponding to the most rapid changes in each component, and continued until 05:50 UT before returning to amplitudes <1 nT/s.

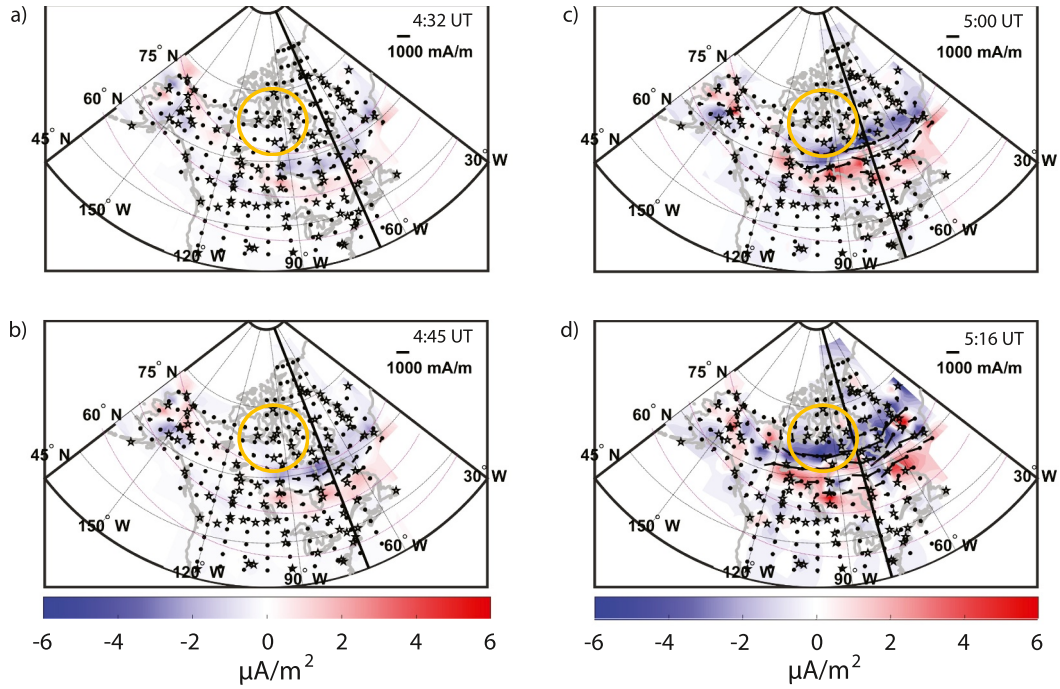

Figure 4. Spherical Elementary Current Systems (SECS) maps of the equivalent ionospheric currents (black arrows) and vertical current intensities (upward in red, downward in blue) across northern North America and western Greenland at 04:32, 04:40, 04: 50, and 05:16 UT. The yellow circle in each map outlines the region of interest. The black lines indicate the midnight local time meridian. The stars show the locations of magnetometers in North America and Greenland providing data for the SECS map on this day, and the dots show the grid points at which the horizontal currents were calculated.

Large variations in the magnetic field at RAN and CDR, located 786 km apart but at similar MLAT, began and ended several minutes earlier (Panels i–k and m–o). Slight drops in Bx near 04:53 UT occurred 1 min after the substorm onset, and rapid drops (negative bay) began at 05:02 UT. Subsequent variations in all three components during the magnetic bay differed in detail at the two stations: they were similar in polarity in Bx and Bz but often opposite in By.

SECS maps (e.g., Figures 4c and 4d) can be used to understand the difference in the By trends at the two stations. As an example, Figures 4c and 4d below show the development of a strong westward equivalent current (a westward electrojet) with a large east-west extent during both the beginning and middle of the negative bay. Its northern edge was near both stations, thus explaining the similarity of the Bx and By components. However, between 04:58 and 05:04 UT (not shown) a localized large poleward-directed equivalent current was evident north of CDR, which would produce the westward (negative) By component there, while only a much weaker northward current was observed farther west at RAN, where only a slight few-minute increase in By was observed during that time.

After 05:30 UT, Bx values at both stations gradually rose toward prior levels. Derivative amplitudes in all three components at both stations increased rapidly at 05:02 UT (panels l and p) and continued until ~05:28 UT before returning to amplitudes <1 nT/s, but peaked at quite different times, again corresponding to the most rapid changes in each component.

Table 2 shows for each of these nine stations the occurrence time, amplitude, and component of the largest GMD and the duration of nearly continuous GMD activity with amplitude >3 nT/s at each station, in order of increasing latitude. This amplitude value was chosen based on the data, but we note that it is intermediate between 1 nT/s and 5 nT/s, two commonly suggested threshold values for generating damaging GICs (Viljanen et al., 2001; Woodroffe et al., 2016). The onset time of intervals of >3 nT/s GMDs at each station was delayed monotonically with increasing latitude, while the times of the peak GMDs at each station showed a similar trend but with much more variability. Table 2 also shows the variability in direction of the largest GMDs: they could appear in any

Table 2
Occurrence Time, Amplitude, and Component of the Largest GMD at Nine Stations, in Order of Increasing Magnetic Latitude, and the Time Span and Duration of Nearly Continuous GMD Activity With Amplitude >3 nT/s

Station	MLAT	Time (UT)	GMD amplitude	Time and duration of >3 nT/s GMDs	
RAN	71.2°	05:19	−10.93 Z	05:02–05:27	25 min
CDR	72.1°	05:23	−9.19 X	05:02–05:28	24 min
CHB	72.4°	05:14	−10.57 X	05:06–05:24	18 min
BLC	72.4°	05:18	18.61 Z	05:10–05:31	21 min
RBY	74.6°	05:23	−10.37 Y	05:19–05:33	14 min
GJO	76.3°	05:30	−19.46 Z	05:24–05:45	21 min
IGL	77.1°	05:28	14.04 X	05:24–05:37	13 min
TAL	77.2°	05:31	9.25 Y	05:24–05:45	21 min
RES	82.0°	05:46	0.81 X	--- ---	0 min

component and with any sign despite the fact that they occurred within the duration of the simultaneous negative bay in Bx; in fact, the two largest GMDs, at BLC and GJO, occurred in the *Z* component, and with opposite signs. This variability suggests that at these magnetic latitudes there is possibly no optimal orientation of long-distance power lines or pipelines that would significantly reduce their susceptibility to the generation of GICs. The time of the onset of continuous >3 nT/s GMD activity appeared first at the two lower latitude stations, and was successively later at higher latitude stations. The duration of continuous activity showed no clear latitudinal or longitudinal pattern. The time of the largest GMD within each interval of continuous GMD activity also varied with no apparent pattern; it could be near the middle or closer to the beginning or end.

Table 3 lists all of the substorm onsets in the Newell and Gjerloev (2011), Forsyth et al. (2015), and Ohtani and Gjerloev (2020) lists available on the SuperMAG web site. The 04:32/04:29 UT onset and the 04:52 UT onset occurred under negative IMF Bz conditions. Both the Newell and Gjerloev and Forsyth et al. lists identified Nain (on the east coast of Labrador) as the location of the 04:32 UT onset, but this onset had negligible effects on the magnetic field at any of the nine stations. The Newell and Gjerloev list identified Fort Churchill as the location of the 04:52 onset. At Fort Churchill (not shown) an isolated −7 nT/s GMD occurred at this time in association with a rapid 200 nT drop in the Bx component, but as noted above, only very gradual onsets of large negative bays were observed at BLC, RAN, CHB, and CDR near this time.

The Newell and Gjerloev list also identified BLC as the location of the 05:17 UT onset, consistent with a rapid ∼250 nT drop in the SML index that occurred during northward IMF conditions. As noted above, onsets of negative bays were observed at GJO, TAL, and IGL at that time. However, the BLC magnetogram Figure S1 in Supporting Information S1 shows that a rapid 350 nT drop in the Bx component at 05:17 UT occurred while Bx was already near the minimum of the negative bay that began near 04:52 UT, so it was associated with a re-intensification of the ongoing substorm and not the onset of a new substorm. This figure also shows an intense GMD (10.0 nT/s in By and 18.6 nT/s in Bz) 2 minutes later at 05:19 UT as the Bx component reached its minimum. Although it may be unusual for such an intensification to occur during northward IMF conditions, this intensification might be related to localized structure in the IMF, or it could instead be caused by belated internal dynamics in the magnetotail following the slightly earlier northward turning of the IMF. No subsequent substorm onsets were listed until ∼08:00 UT. We also note that each of the large GMDs listed in Table 2 occurred between 05:14 and 05:31 UT, that is, with a delay of ≥22 min after the closest previous substorm onset at 04:52 UT.

3.3. SECS Maps and Auroral Images

Figures 4 and 6 show maps of equivalent ionospheric currents and vertical current intensities (a proxy for field-aligned currents) across northern North America using the Spherical Elementary Current Systems (SECS) method (Amm, 1997; Amm & Viljanen, 1999; Amm et al., 2002) produced using all available ground-based magnetometers in northern North America and western Greenland (Weygand, 2009a, 2009b; Weygand et al., 2011).

The SECS method first produces the equivalent ionospheric currents by removing a background magnetic field from the ground magnetometers and then inverting the remaining magnetic field fluctuations through singular value decomposition to obtain the equivalent currents. Auroral images and particle precipitation data indirectly indicate that the ionospheric conductivity is non-uniform, but the distribution or values of the conductivity are not needed to obtain the equivalent currents. The second part of the SECS method is to obtain the curl-free currents, which the SECS method refers to as current amplitudes (field-aligned-like currents), because they are vertical currents derived at predetermined ionospheric grid points. These current amplitudes are calculated from the curl of the equivalent ionospheric currents. To obtain these results from Ohm's law in the ionosphere, two assumptions are made.

Table 3
Substorm Onsets Immediately Before, During, and After the Time Interval From 04:30 to 06:00 UT on 28 November 2022 Included in the Newell and Gjerloev (2011), Forsyth et al. (2015), and Ohtani and Gjerloev (2020) Substorm Lists Available on the SuperMAG Web Site

List	Date	Time	Time	Time	Time	Time	Times
Newell & Gjerloev	11/28	03:27	04:32	04:52	05:17		09:05
Forsyth et al.	11/28	03:11	04:29			08:01	09:05
Ohtani & Gjerloev	11/28	03:26				07:56	

The first assumption is that the Hall to Pedersen conductance ratio is constant: $\alpha = \Sigma_H/\Sigma_P = constant$ where Σ_H and Σ_P are the height integrated Hall and Pedersen conductivities. The second assumption is that $\left(\nabla\Sigma_H \times \vec{E}\right)_r = 0$, where $\vec{E}$ is the convection electric field. From these two assumptions, Ohm's law can be simplified and the current amplitudes can be written as

$$j_{df,r} = \nabla \cdot \vec{J} = -\frac{1}{\alpha}\left(\nabla \times \vec{J}_{df}\right)$$

where $\vec{J}_{df}$ is the divergence free current (equivalent current) and $j_{df,r}$ is the current amplitude (vertical current/field aligned like current). For more details on the derivation, see Amm et al. (2002), Juusola et al. (2009), and Vanhamäki and Amm (2011).

Figure 4 shows SECS maps at four times near the beginning of this interval. The stars show the locations of magnetometers providing data on this day, and the dots show the grid points at which the horizontal currents were calculated. The maps are most accurate in regions with dense magnetometer coverage. The yellow circle in each of these maps outlines the region of interest. It is centered over the locations of GJO and TAL; BLC and RAN are near the bottom, and CDR is just outside the circle at the lower right. At 04:32 UT, the time of the first identified substorm onset in Figure 2, and before the appearance of any magnetic bay, Figure 4a shows only weak and mostly northward equivalent currents in this region. To the south, an extended east-west region of downward vertical current (blue) separated the circled region from a narrow region of westward equivalent currents extending from Greenland to central Canada. Four patches of upward vertical current (red) were located beneath and slightly equatorward of the westward currents. By 04:45 UT (Figure 4b) the extended vertical current region had moved slightly northward, and the westward equivalent current region had both broadened and intensified. By 05:00 UT (Figure 4c), the upward current region had intensified and reached northward over RAN and CDR, and the regions of westward and upward currents also had intensified and moved northward (note the factor of two change in scale for panels c and d). Between 05:09 and 05:11 UT, the SML index showed a ∼150 nT downward spike (Figure 2f), and both regions moved rapidly poleward (not shown). By 5:16 UT (Figure 4d), near the time of the minima in the Bx components at RAN and CDR, an even more intense longitudinally extended band of downward current stretched between BLC and GJO, and southward of it an even stronger and slightly wider westward electrojet was present. Throughout the period between 04:20 and 05:16 UT, the equivalent currents at GJO, TAL, and IGL remained weak and mostly northward.

Four additional SECS maps at times after the IMF turned strongly northward and antisunward are shown in Figure 6. We comment here only on the first of these, at 05:24 UT (Figure 6a), ∼9 min after the IMF turned strongly northward. By this time, patches of upward current had moved to the north and west of GJO and TAL, and south-southwest-directed equivalent current vectors reached just south of these stations. Also, at this time, GMDs at GHO and TAL suddenly increased in amplitude to 20 and 10 nT/s (Figures 3d and 3h), respectively.

Figure 5 shows simultaneous zoomed-in SECS maps of equivalent ionospheric and vertical currents and all-sky camera images from the TAL imager at 05:16, 05:30, 05:31, and 05:32 UT. The field of view of the imager corresponds closely to the circled region, as can be seen by comparing the background outlines of land masses and the symbols identifying station locations. Figure 5a, a zoomed-in version of Figure 4d, shows more clearly the spatial separation between the region of westward currents at the southern edge of the circled region and the very weak and mostly northward currents in the northern half of that region. Figure 5e shows no auroral activity above GJO and TAL in the middle of the imager's field of view. The bright regions at the eastern and west-northwestern edges of the image are caused by light pollution from the town. A bright region at the southeastern edge shows activity east of RBY and north of CHB as well as weak activity north of RAN and BLC.

A more complex system of horizontal and vertical currents is evident in Figures 5b–5d, at 05:30, 05:31, and 05:32 UT, spanning the time of the largest GMDs observed at GJO and TAL (Figures 3d and 3h) and near the time of the Bx minima at these stations. The auroral images during these times (Figures 5f–5h) correspond to a bright poleward boundary intensification (PBI) during the substorm poleward expansion. At 05:30 UT, patches of downward current remained to the north and west of GJO and TAL, and a localized region of up to 6.1 μA/m^2 upward current appeared at its southern edge, above BLC. Figure 5f shows a bright arc extending from the southwest toward GJO as well as weak narrow arcs extending from it to GJO and TAL. This bright arc appears to be located in the middle of the strong westward equivalent current. One minute later, at 05:31 UT (Figure 5c), the

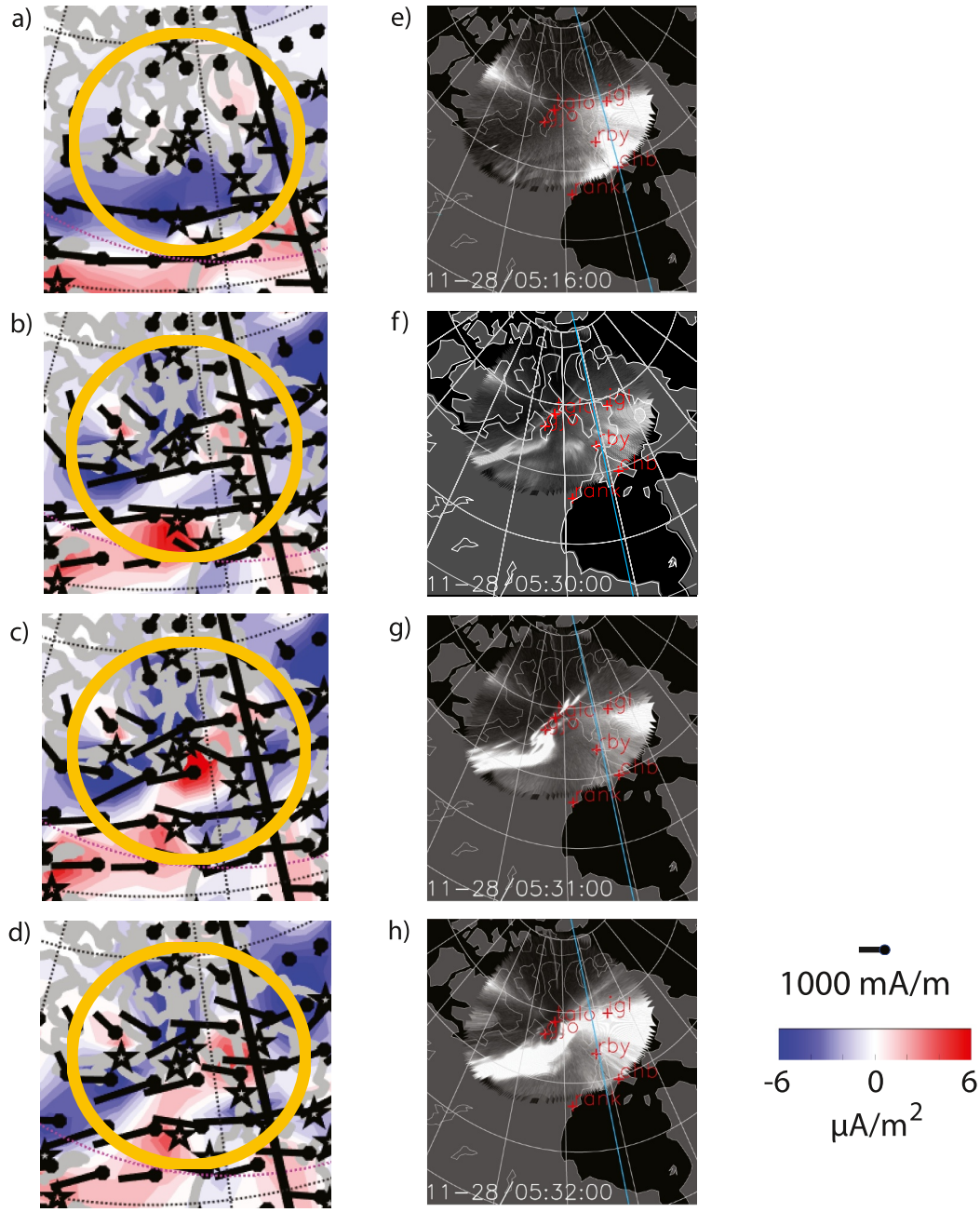

Figure 5. Left: Zoomed-in SECS maps of equivalent ionospheric and vertical currents at (a) 05:16 UT, (b) 05:30 UT, (c) 05:31 UT, and (d) 05:32 UT 28 November 2022. The circled region is the same as in Figure 4. Center: all-sky camera images from the Taloyoak imager (e–h) at these same times. The field of view of the imager corresponds closely to the circled region. Right: Scales for the SECS maps: horizontal equivalent current density (in mA/m) and vertical current density (in $\mu A/m^2$).

upward currents (blue) moved slightly more toward the north and west of GJO and TAL, a localized region of 8.3 $\mu A/m^2$ upward current (red) was located to the southeast of and very close to these stations, and the northern edge of a bright arc was located over GJO (Figure 5g). The PBI includes a surge (vortical auroral form) just to the south of the GJO, and it is likely associated with an enhanced upward current and a distortion of the horizontal current. By 05:32 UT (Figure 5d), the downward current regions were mostly the same, but the intense upward

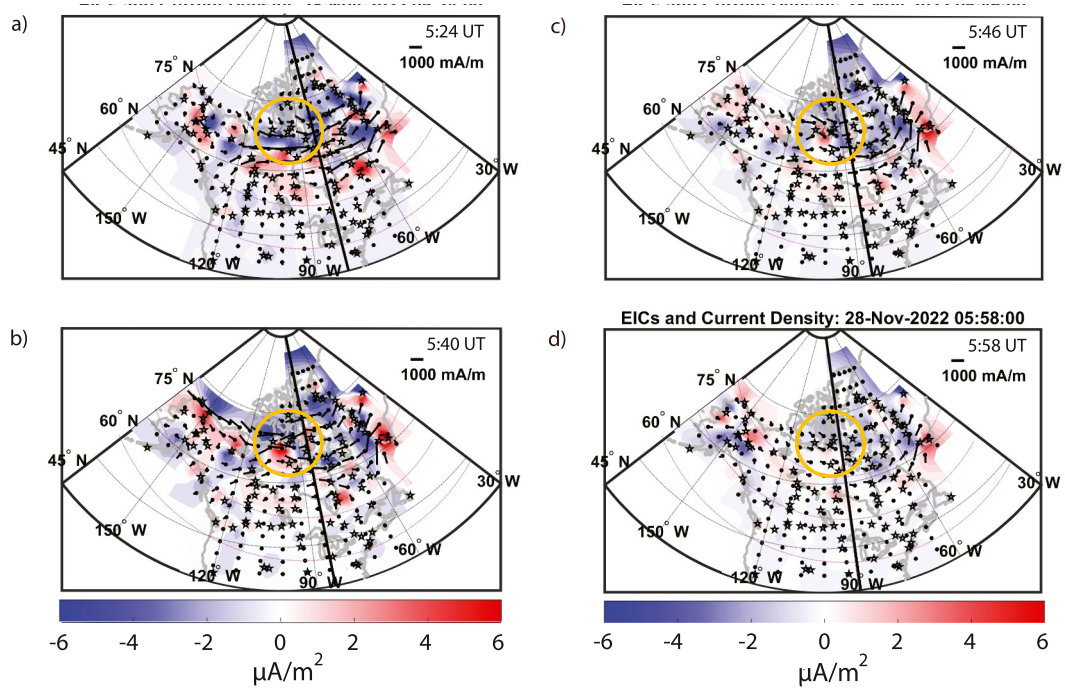

Figure 6. Spherical Elementary Current Systems (SECS) maps of the equivalent ionospheric currents and vertical current intensities across northern North America and western Greenland as in Figure 4, but at 05:24, 05:40, 05: 46, and 05:58 UT.

current region near GJO and TAL had disappeared, and the edge of the bright auroral arc had moved southeast of GJO and TAL.

SECS maps at 10-s time intervals from 05:30 to 05:32 UT (Figure S6 in Supporting Information S1) indicated that the blue region just north of TAL was nearly stationary and had constant intensity during these two minutes, but the red region south of GJO grew in intensity from about 0.75 μA/m^2 at 05:30 to about 2.2 μA/m^2 at 05:30:30 UT, expanded to southeast of GJO at 05:30:40 UT, intensified to 3.6 μA/m^2 and moved closer to GJO at 05:30:50 UT, and intensified further to 8.3 μA/m^2 at 05:31:00 UT while remaining in place. The red region remained nearly constant in intensity and location through 05:31:30 UT but dropped to 3.7 μA/m^2 by 05:31:40 UT, 2.8 μA/m^2 by 05:31:50 UT, and 2.2 μA/m^2 by 05:32:00 UT, indicating a lifetime of the localized upward current region of <2 min.

We now return to the later effects of the strongly northward IMF orientation on the latitudinal extent of equivalent and vertical currents, as shown by SECS maps at 05:40, 05:46, and 05:58 UT (Figures 6b–6d). At 05:40 UT (Figure 6b), the westward electrojet reached its highest latitude just south of RES, and it covered nearly all latitudes enclosed in the yellow circle. Between 05:32 and 05:40 UT, GMDs at GJO and TAL continued to occur, but with peak amplitudes mostly near 4 nT/s (Figures 3d and 3h). Only one GMD at TAL (05:35 UT) exceeded 5 nT/s. Figure S5 in Supporting Information S1 shows that at Resolute Bay, a shallow negative bay in the Bx component at RES began near 05:22 UT, reached its minimum at 05:40 UT as the westward electrojet reached its highest latitude, and returned to its previous value by 06:00 UT.

The IMF Bz component dropped to +2 nT by 05:45 UT. Shortly thereafter, at 05:46 UT (Figure 6c) the westward electrojet began to recede southward, the amplitude of GMDs at GJO and TAL began to drop toward 1 or 2 nT/s, the negative bay in the Bx component at GJO had returned to nearly its previous undisturbed level, but the negative bay at TAL had returned only by ~40%. At 05:50 UT, the IMF Bz component became negative, and by 05:58 UT, as shown in Figure 6d, the northern edge of a considerably weaker westward electrojet was only slightly north of GJO and TAL and all three components of B at both stations had returned to nearly their prior 04:30 UT levels.

4. Connection to Earlier Studies

This study supplements several prior studies with two new observations. First, GMDs exceeding 9 nT/s appeared over a large region and, to our knowledge, at the highest yet reported magnetic latitudes during an interval of high Vsw but only moderately large SML and SYM/H values. Second, because extended exposures to GMDs as well as to much shorter intervals of large amplitude dB/dt are understood to cause GICs that can damage technological infrastructure, we have documented the duration of intervals of continuous >3 nT/s GMDs, and demonstrated that the largest GMDs occurred at various times during these intervals.

This is not the first report of large-amplitude, poleward-moving GMDs. In the two storm-time events presented by Ngwira et al. (2018), with Vsw ∼710 and ∼500 km/s, respectively, intense *dB*/*dt* events appeared within the auroral zone and moved poleward as the auroral oval expanded poleward. Ngwira et al. showed the association between intense *dB*/*dt* and the poleward moving arc along the poleward boundary of the bulge, and cautioned that it is not clear that substorms are themselves the primary seeding mechanism for strong *dB*/*dt* events, because substorms are widespread in nature but extreme *dB*/*dt* events are localized. The major difference from their events, however, is that the strong *dB*/*dt* in the present paper occurs near the poleward boundary of the auroral oval associated with a large PBI. The poleward progression of GMDs was also shown in the first of three multi-station events presented by Engebretson et al. (2019) with MLAT ranging from 67.7° to 77.6° (their Figure 4 showed intense currents were associated with the auroral surge along the poleward boundary), and by McCuen et al. (2023) with MLAT ranging from 62.4° to 75.3°. Both of these events also occurred during periods of large Vsw, 665 and 685 km/s, respectively. The relation to the PBI in the present study is analogous to the results shown by Engebretson et al. and McCuen et al., but the PBI in our event is more localized with only a small poleward expansion, suggesting a confined magnetospheric source region. A similarly large-scale GMD event was presented by Wei et al. (2021) with MLAT ranging from 59° to 74°, but the largest GMDs observed were 7.2 and 6.6 nT/s, and Vsw during this event was ∼460 km/s (still above the long-term median value). Mention can also be made of the supersubstorm event studied by Nishimura et al. (2020); although this study did not focus on dB/dt values, it provided additional evidence of how intense currents evolve toward the poleward boundary at high latitudes. This event also occurred during an interval of high Vsw (>700 km/s).

Earlier studies by Zesta et al. (2000, 2006) found that intensifications of substorm-related auroras at their poleward boundaries (PBIs) correlated well with plasma sheet fast flows observed within the same local time sector. Lyons et al. (2012) investigated several large plasma sheet dipolarization fronts or dipolarizing flux bundles, DFBs (the components of bursty bulk flows) identified by Runov et al. (2009, 2011) and found that many of these events occurred during the substorm expansion phase after onset and were related to auroral streamers. Lyons et al. (2012) also noted that the auroral zone ground magnetic field showed only modest responses to substorm onsets but abrupt and large responses to post-onset dipolarization-front-related streamers.

Panov et al. (2019) compared observations of DFBs that were observed by THEMIS spacecraft during non-substorm times in the near magnetotail to observations by magnetically conjugate all-sky imagers and magnetometer networks near THEMIS magnetic footpoints, and showed that localized and short-lived intensifications of up/down current pairs, westward electrojet currents, and auroral bright spots occurred near THEMIS footpoints during each DFB. They did not, however, make explicit connections to the occurrences of GMDs.

Wei et al. (2021) study was the first to provide evidence directly connecting GMDs to bursty bulk flows. It combined BBF data from Cluster, field-aligned current data from the low-altitude Swarm satellites, and observations of a train of GMDs from stations in central Canada for an interval during the 7 January 2015 geomagnetic storm. Recently, Engebretson, Gaffaney, et al. (2024) identified DFBs observed in the midnight sector from ∼7 to ∼10 R_E by THEMIS A, D, and E during days in 2016–2017 whose northern hemisphere magnetic footpoints mapped to regions near Hudson Bay, Canada, and compared them to isolated GMDs observed by ground magnetometers. This study identified 6 days during which one or more of these DFBs coincided to within ±3 min with ≥6 nT/s GMDs observed by latitudinally closely spaced ground-based magnetometers located near those footpoints. On all but one of these days, Vsw exceeded 500 km/s. Ngwira et al. (2025) presented a similar example during the early phase of a magnetic storm. Unfortunately, during the event reported here there were no conjunctions with Geotail, Cluster, THEMIS A, D, or E satellite passages through the near magnetotail, so this study cannot provide any evidence directly linking these GMDs to any drivers in the magnetotail.

Several studies have found that the auroral structures associated with localized fast flows in the magnetotail fall into two main categories: auroral streamers and transient auroral bright spots. Nakamura et al. (2001) found that BBFs observed by Geotail corresponded either to localized auroral intensifications associated with small poleward expansions and pseudobreakups or to auroral streamers. Panov et al. (2019) compared observations of DFBs that were observed by THEMIS spacecraft during non-substorm times amidst azimuthally drifting interchange heads (depleted plasma tubes) in the near magnetotail to observations by magnetically conjugate all-sky images and magnetometer networks near THEMIS magnetic footpoints. Although this study focused on the association of interchange heads with DFBs, it also showed that localized and short-lived intensifications of up/down current pairs, westward electrojet currents, and auroral bright spots occurred near THEMIS footpoints during each DFB. Both of these studies observed features consistent with those reported here, but neither study made explicit connections to the occurrence of GMDs. As noted in the introduction, more recent papers by Weygand et al. (2022), McCuen et al. (2023), and Engebretson, Gaffaney, et al. (2024) made such connections.

5. Summary and Conclusions

Using a combination of data from nine ground magnetometers located in a large region north of Hudson Bay, Canada, all-sky imager data, and SECS maps, we have observed a geographically extended interval of very large geomagnetic disturbances and their association with the drivers and indices of large-scale geomagnetic activity as well as with nearby and overhead auroras and mesoscale equivalent ionospheric and vertical currents. Distinct small-scale and rapidly changing ionospheric structures were embedded within these regions.

1. Greater than 9 nT/s geomagnetic disturbances (GMDs) were observed at eight high-latitude sites over a large region in Arctic Canada during a high-speed solar wind stream but under moderately disturbed auroral and storm conditions.
2. GMDs occurred near the poleward edge of the auroral zone in two stages during the expansion phases of a substorm: first near 72° MLAT and 10–20 min later near 77° MLAT.
3. Sustained >3 nT/s GMD activity appeared at each station with durations from 13 to 25 min during magnetic bays.
4. The strongest GMDs occurred at various times during these intervals of sustained GMDs.
5. SECS maps revealed that GMDs were associated with highly localized and short-lived up/down current pairs and localized electrojet currents. In particular, we noted the rapid appearance and subsequent disappearance of a localized and stationary upward current region very near Gjoa Haven between 05:30 and 05:32 UT.

Although there have been an increasing number of studies of the largest GICs and/or their GMD drivers over a wide range of latitudes and under varying geomagnetic conditions, we note that there has been less focus on the temporal extent of potentially dangerous GMDs. We hope that future studies in regions more susceptible to large GICs will also document the duration of moderate to large GMDs and attempt to assess the possible longer-term damage to power systems that they may cause.

Data Availability Statement

Ground-based magnetometer data from the MACCS and CARISMA arrays used in this study can be accessed at Engebretson et al. (2011) and Mann et al. (2023), respectively. CANMOS data from BLC and British Geological Survey data from RES are available from the Intermagnet web site, https://imag-data.bgs.ac.uk/GIN_V1/GINForms2. THEMIS all sky imager data from RAN and TAL are available from the THEMIS web site (Mende, 2004). SECS maps at a 1-min cadence are available at http://vmo.igpp.ucla.edu/data1/SECS/Quicklook/; higher time resolution maps are available on demand from James Weygand. The SuperMAG SML and SMU indices and substorm lists accessed in this study are available from the SuperMAG web site (Gjerloev, 2012, 2023).

Acknowledgments

This research was supported by National Science Foundation Grants AGS-2013648 to Augsburg University and AGS-2013433 to the University of Michigan. Work by JMW was supported by NASA Grants HSR-80NSSC18K1227 and SWO2R 80NSSC20K1364, NASA contract HPDE-80GSFC17C0018, NSF Grant GEO-NERC 2027190, GEM-2400140, and NSF Grant AGS-2013648 via subcontract from Augsburg University. Work by Yukitoshi Nishimura was supported by NASA Grants 80NSSC18K0657, 80NSSC20K0604, 80NSSC20K0725, 80NSSC21K1321, 80NSSC22K0323, and 80NSSC22M0104, NSF Grants AGS-1907698 and AGS-2100975, and AFOSR Grant FA9559-16-1-0364. We thank Ian Mann, D. K. Milling, A. Kale and the rest of the CARISMA team for data. CARISMA is operated by the University of Alberta and funded by the Canadian Space Agency. THEMIS all-sky imagers are supported by NASA NAS5-02099. We gratefully acknowledge the SuperMAG collaborators (https://supermag.jhuapl.edu/info/?page=acknowledgement).

References

Akasofu, S.-I. (1964). The development of the auroral substorm. *Planetary and Space Science*, *12*, 273–282. https://doi.org/10.1016/0032-0633(64)90151-5

Akasofu, S. I. (2004). Several "controversial" issues on substorms. *Space Science Reviews*, *113*, 1–40. https://doi.org/10.1023/B:SPAC.0000042938.57710.fb

Amm, O. (1997). Ionospheric elementary current systems in spherical coordinates and their application. *Journal of Geomagnetism and Geoelectricity*, *49*(7), 947–955. https://doi.org/10.5636/jgg.49.947

Amm, O., Engebretson, M. J., Hughes, T., Newitt, L., Viljanen, A., & Watermann, J. (2002). A traveling convection vortex event study: Instantaneous ionospheric equivalent currents, estimation of field-aligned currents, and the role of induced currents. *Journal of Geophysical Research*, *107*(A11), SIA1-1–SIA1-11. https://doi.org/10.1029/2002JA009472

Amm, O., & Viljanen, A. (1999). Ionospheric disturbance magnetic field continuation from the ground to the ionosphere using spherical elementary currents systems. *Earth Planets and Space*, *51*(6), 431–440. https://doi.org/10.1186/BF03352247

Boteler, D. H. (2019). A 21st century view of the March 1989 magnetic storm. *Space Weather*, *17*, 1427–1441. https://doi.org/10.1029/2019SW002278

Carrington, R. C. (1859). Description of a singular appearance seen in the Sun on September 1, 1859. *Monthly Notices of the Royal Astronomical Society*, *20*, 13–15. https://doi.org/10.1093/mnras/20.1.13

Despirak, I. V., Lyubchich, A. A., & Kleimenova, N. G. (2014). Polar and high latitude substorms and solar wind conditions. *Geomagnetism and Aeronomy*, *54*, 575–582. https://doi.org/10.1134/S0016793214050041

Donovan, E., Mende, S. B., Jackel, B., Frey, H. U., Syrjasuo, M., Voronkov, I., et al. (2006). The THEMIS all-sky imaging array—System design and initial results from the prototype imager. *Journal of Atmospheric and Solar-Terrestrial Physics*, *68*(13), 1472–1487. https://doi.org/10.1016/j.jastp.2005.03.027

Doolittle, J. H., Mende, S. B., Frey, H. U., Rosenberg, T. J., Weatherwax, A. T., Lanzerotti, L. J., et al. (1998). Substorm auroral expansion to high latitudes and the dawn/dusk flanks. In S. Kokubun & Y. Kamide (Eds.), *Substorms-4: International Conference on Substorm-4, Lake Hamana, Japan* (pp. 47–50). Terra Scientific Publishing Company.

Engebretson, M., Steinmetz, E., & Moldwin, M. (2011). MACCS 0.5 s Ground Magnetometer Data [Dataset]. Augsburg University. https://doi.org/10.48322/sydj-ab90

Engebretson, M. J., Gaffaney, S. A., Ochoa, J. A., Runov, A., Weygand, J. M., Nishimura, Y., et al. (2024). Signatures of dipolarizing flux bundles in the nightside auroral zone. *Journal of Geophysical Research: Space Physics*, *129*, e2023JA032266. https://doi.org/10.1029/2023JA032266

Engebretson, M. J., Hughes, W. J., Alford, J. L., Zesta, E., Cahill, L. J., Jr., Arnoldy, R. L., & Reeves, G. D. (1995). Magnetometer array for cusp and cleft studies observations of the spatial extent of broadband ULF magnetic pulsations at cusp/cleft latitudes. *Journal of Geophysical Research*, *100*, 19371–19386. https://doi.org/10.1029/95JA00768

Engebretson, M. J., Steinmetz, E. S., Posch, J. L., Pilipenko, V. A., Moldwin, M. B., Connors, M. G., et al. (2019). Nighttime magnetic perturbation events observed in Arctic Canada: 2. Multiple-Instrument observations. *Journal of Geophysical Research: Space Physics*, *124*(9), 7459–7476. https://doi.org/10.1029/2019JA026797

Engebretson, M. J., Yang, L., Steinmetz, E. S., Pilipenko, V. A., Moldwin, M. B., McCuen, B. A., et al. (2024). Extreme geomagnetic disturbances (GMDs) observed in Eastern Arctic Canada: Occurrence characteristics and solar cycle dependence. *Journal of Geophysical Research: Space Physics*, *129*, e2023JA031643. https://doi.org/10.1029/2023JA031643

Fairfield, D. H., & Cahill, L. J., Jr. (1966). Transition region magnetic field and polar magnetic disturbances. *Journal of Geophysical Research*, *71*, 155–169. https://doi.org/10.1029/JZ071i001p00155

Forsyth, C., Rae, I. J., Coxon, J. C., Freeman, M. P., Jackman, C. M., Gjerloev, J., & Fazakerley, A. N. (2015). A new technique for determining Substorm Onsets and Phases from Indices of the Electrojet (SOPHIE). *Journal of Geophysical Research: Space Physics*, *120*, 10592–10606. https://doi.org/10.1002/2015JA021343

Gjerloev, J. W. (2012). The SuperMAG data processing technique. *Journal of Geophysical Research*, *117*, A09213. https://doi.org/10.1029/2012JA017683

Gjerloev, J. W. (2023). SuperMAG, global magnetic field observations and products made possible by the contributors [Dataset]. *Applied Physics Laboratory*. Retrieved from https://supermag.jhuapl.edu/

Gussenhoven, M. S. (1982). Extremely high latitude auroras. *Journal of Geophysical Research*, *87*, 2401–2412. https://doi.org/10.1029/JA087iA04p02401

Hapgood, M. (2019). The great storm of May 1921: An exemplar of a dangerous space weather event. *Space Weather*, *17*, 950–975. https://doi.org/10.1029/2019SW002195

Juusola, L., Nakamura, R., Amm, O., & Kauristie, K. (2009). Conjugate ionospheric equivalent currents during bursty bulk flows. *Journal of Geophysical Research*, *114*, A04313. https://doi.org/10.1029/2008JA013908

Kellinsalmi, M., Viljanen, A., Juusola, L., & Käki, S. (2022). The time derivative of the geomagnetic field has a short memory. *Annales Geophysicae*, *40*, 545–562. https://doi.org/10.5194/angeo-40-545-2022

Kisabeth, J. L., & Rostoker, G. (1974). The expansive phase of magnetospheric substorms: 1. Development of the auroral electrojets and auroral arcs configuration during a substorm. *Journal of Geophysical Research*, *79*, 972–984. https://doi.org/10.1029/JA079i007p00972

Love, J. J., Hayakawa, H., & Cliver, E. W. (2019). Intensity and impact of the New York Railroad superstorm of May 1921. *Space Weather*, *17*, 1281–1292. https://doi.org/10.1029/2019SW002250

Lyons, L. R., Nishimura, Y., Xing, X., Runov, A., Angelopoulos, V., Donovan, E., & Kikuchi, T. (2012). Coupling of dipolarization front flow bursts to substorm expansion phase phenomena within the magnetosphere and ionosphere. *Journal of Geophysical Research*, *117*, A02212. https://doi.org/10.1029/2011JA017265

Mann, I. R., Milling, D. K., & Kale, A. (2023). CARISMA magnetometer network [Dataset]. *University of Alberta*. Retrieved from https://carisma.ca

Mann, I. R., Milling, D. K., Rae, I. J., Ozeke, L. G., Kale, A., Kale, Z. C., et al. (2008). The upgraded CARISMA magnetometer array in the THEMIS era. *Space Science Reviews*, *141*(1-4), 413–451. https://doi.org/10.1007/s11214-008-9457-6

Marshall, R. A., Smith, E. A., Francis, M. J., Waters, C. L., & Sciffer, M. D. (2011). A preliminary risk assessment of the Australian region power network to space weather. *Space Weather*, *9*, S10004. https://doi.org/10.1029/2011SW000685

McCuen, B. A., Moldwin, M. B., Engebretson, M. J., Weygand, J. M., & Nishimura, Y. (2023). Magnetosphere–ionosphere drivers of transient-large amplitude geomagnetic disturbances: Statistical analysis and event study. *Journal of Geophysical Research: Space Physics*, *128*, e2023JA031587. https://doi.org/10.1029/2023JA031587

Mende, S. B. (2004). THEMIS all sky imager data [Dataset]. *University of California*. Retrieved from http://themis.ssl.berkeley.edu/themisdata/thg/l1/asi/

Mende, S. B., Harris, S. E., Frey, H. U., Angelopoulos, V., Russell, C. T., Donovan, E., et al. (2008). The THEMIS array of ground-based observatories for the study of auroral substorms. *Space Science Reviews*, *141*, 357–387. https://doi.org/10.1007/978-0-387-89820-9_16

Milan, S., Imber, S., Fleetham, A., & Gjerloev, J. (2023). Solar cycle and solar wind dependence of the occurrence of large dB/dt events at high latitudes. *Journal of Geophysical Research: Space Physics*, *128*, e2022JA030953. https://doi.org/10.1029/2022JA030953

Nakamura, R., Baumjohann, W., Brittnacher, M. M., Sergeev, V. A., Kubyshkina, M., Mukai, T., & Liou, K. (2001). Flow bursts and auroral activations: Onset timing and foot point location. *Journal of Geophysical Research*, *106*, 10777–10789. https://doi.org/10.1029/2000JA000249

National Academies of Sciences, Engineering, and Medicine. (2024). *The next decade of discovery in solar and space physics: Exploring and safeguarding humanity's home in space*. The National Academies Press. https://doi.org/10.17226/27938

Newell, P. T., & Gjerloev, J. W. (2011). Evaluation of SuperMAG auroral electrojet indices as indicators of substorms and auroral power. *Journal of Geophysical Research*, *116*, A12211. https://doi.org/10.1029/2011JA016779

Ngwira, C. M., Nishimura, Y., Weygand, J. M., Engebretson, M. J., Pulkkinen, A., & Schuck, P. W. (2025). Observations of localized horizontal geomagnetic field variations associated with a magnetospheric fast flow burst during a magnetotail reconnection event detected by the THEMIS spacecraft. *Journal of Geophysical Research: Space Physics*, *130*, e2024JA032651. https://doi.org/10.1029/2024JA032651

Ngwira, C. M., & Pulkkinen, A. A. (2019). An introduction to geomagnetically induced currents. In J. L. Gannon, A. Swidinsky, & Z. Xu (Eds.), *Geomagnetically induced currents from the Sun to the power grid, Geophysical Monograph Series* (Vol. 244, pp. 3–13). American Geophysical Union. https://doi.org/10.1002/9781119434412.ch1

Ngwira, C. M., Sibeck, D., Silveira, M. V. D., Georgiou, M., Weygand, J. M., Nishimura, Y., & Hampton, D. (2018). A study of intense local dB/dt variations during two geomagnetic storms. *Space Weather*, *16*. https://doi.org/10.1029/2018SW001911

Nikitina, L., Trichtchenko, L., & Boteler, D. H. (2016). Assessment of extreme values in geomagnetic and geoelectric field variations for Canada. *Space Weather*, *14*, 481–494. https://doi.org/10.1002/2016SW001386

Nishimura, Y., Lyons, L. R., Gabrielse, C., Sivadas, N., Donovan, E. F., Varney, R. H., et al. (2020). Extreme magnetosphereionosphere-thermosphere responses to the 5 April 2010 supersubstorm. *Journal of Geophysical Research: Space Physics*, *125*, e2019JA027654. https://doi.org/10.1029/2019JA027654

Ohtani, S., & Gjerloev, J. W. (2020). Is the substorm current wedge an ensemble of wedgelets? Revisit to midlatitude positive bays. *Journal of Geophysical Research: Space Physics*, *125*, e2020JA027902. https://doi.org/10.1029/2020JA027902

Panov, E. V., Baumjohann, W., Nakamura, R., Pritchett, P. L., Weygand, J. M., & Kubyshkina, M. V. (2019). Ionospheric footprints of detached magnetotail interchange heads. *Geophysical Research Letters*, *46*(13), 7237–7247. https://doi.org/10.1029/2019GL083070

Runov, A., Angelopoulos, V., Sitnov, M. I., Sergeev, V. A., Bonnell, J., McFadden, J. P., et al. (2009). THEMIS observations of an earthward propagating dipolarization front. *Geophysical Research Letters*, *36*, L14106. https://doi.org/10.1029/2009GL038980

Runov, A., Angelopoulos, V., Zhou, X.-Z., Zhang, X.-J., Li, S., Plaschke, F., & Bonnell, J. (2011). A THEMIS multicase study of depolarization fronts in the magnetotail plasma sheet. *Journal of Geophysical Research*, *116*, A05216. https://doi.org/10.1029/2010JA016316

Shi, X., Hartinger, M. D., Zou, Y., Rigler, E. J., Weygand, J. M., Kelbert, A., et al. (2025). Multi-scale intense geoelectric and geomagnetic field perturbations observed after an interplanetary magnetic field turning. *Space Weather*, *23*, e2024SW004046. https://doi.org/10.1029/2024SW004046

Troshichev, O. A., Kuznetsov, B. M., & Pudovkin, M. J. (1974). The current systems of the magnetic substorm growth and explosive phases. *Planetary and Space Science*, *22*, 1403–1412.

Vanhamäki, H., & Amm, O. (2011). Analysis of ionospheric electrodynamic parameters on mesoscales—A review of selected techniques using data from ground-based observation networks and satellites. *Annales Geophysicae*, *29*, 467–491. https://doi.org/10.5194/angeo-29-467-2011

Viljanen, A., Nevanlinna, H., Pajunpää, K., & Pulkkinen, A. (2001). Time derivative of the horizontal geomagnetic field as an activity indicator. *Annales Geophysicae*, *19*, 1107–1118. https://doi.org/10.5194/angeo-19-1107-2001

Wei, D., Dunlop, M. W., Yang, J., Dong, X., Yu, Y., & Wang, T. (2021). Intense *dB/dt* variations driven by near-Earth bursty bulk flows (BBFs): A case study. *Geophysical Research Letters*, *48*(4), e2020GL091781. https://doi.org/10.1029/2020GL091781

Weygand, J. M. (2009a). *Equivalent ionospheric currents (EICs) derived using the spherical elementary currrent systems (SECS) technique at 10 s resolution in geographic coordinates*. University of California. https://doi.org/10.21978/P8D62B

Weygand, J. M. (2009b). Spherical elementary current (SEC) amplitudes derived using the spherical elementary currents systems (SECS) technique at 10 sec resolution in geographic coordinates. *UCLA*. https://doi.org/10.21978/P8PP8X

Weygand, J. M., Amm, O., Viljanen, A., Angelopoulos, V., Murr, D., Engebretson, M. J., et al. (2011). Application and validation of the spherical elementary currents systems technique for deriving ionospheric equivalent currents with the North American and Greenland ground magnetometer arrays. *Journal of Geophysical Research*, *116*(A3), A03305. https://doi.org/10.1029/2010JA016177

Weygand, J. M., Bortnik, J., Chu, X., Cao, X., Li, J., Aryan, H., & Tian, S. (2022). Magnetosphere-ionosphere coupling between north-south propagating streamers and high-speed earthward flows. *Journal of Geophysical Research: Space Physics*, *127*(10), e2022JA030741. https://doi.org/10.1029/2022JA030741

Weygand, J. M., Engebretson, M. J., Pilipenko, V. A., Steinmetz, E. S., Moldwin, M. B., Connors, M. G., et al. (2021). SECS analysis of nighttime magnetic perturbation events observed in Arctic Canada. *Journal of Geophysical Research: Space Physics*, *126*(11), e2021JA029839. https://doi.org/10.1029/2021JA029839

Woodroffe, J. R., Morley, S. K., Jordanova, V. K., Henderson, M. G., Cowee, M. M., & Gjerloev, J. G. (2016). The latitudinal variation of geoelectromagnetic disturbances during large ($Dst \leq -100$ nT) geomagnetic storms. *Space Weather*, *14*, 668–681. https://doi.org/10.1002/2016SW001376

Zesta, E., Lyons, L., & Donovan, E. (2000). The auroral signature of earthward flow bursts observed in the magnetotail. *Geophysical Research Letters*, *27*, 3241–3244. https://doi.org/10.1029/2000GL000027

Zesta, E., Lyons, L., Wang, C.-P., Donovan, E., Frey, H., & Nagai, T. (2006). Auroral poleward boundary intensifications (PBIs): Their two dimensional structure and associated dynamics in the plasma sheet. *Journal of Geophysical Research*, *111*, A05201. https://doi.org/10.1029/2004JA010640